The Peculiar Debris Disk of HD 111520 as Resolved by the Gemini Planet Imager

Zachary H. Draper, Gaspard Duchêne, Maxwell A. Millar-Blanchaer, Brenda C. Matthews, Jason J. Wang, Paul Kalas, James R. Graham, Deborah Padgett, S. Mark Ammons, Joanna Bulger, et al.

The Astrophysical Journal, 826:147 (9pp), 2016 August 1 doi:10.3847/0004-637X/826/2/147

THE PECULIAR DEBRIS DISK OF HD 111520 AS RESOLVED BY THE GEMINI PLANET IMAGER

Zachary H. Draper[1,2], Gaspard Duchêne[3,4], Maxwell A. Millar-Blanchaer[5,6], Brenda C. Matthews[1,2], Jason J. Wang[3], Paul Kalas[3], James R. Graham[3], Deborah Padgett[7], S. Mark Ammons[8], Joanna Bulger[9], Christine Chen[10], Jeffrey K. Chilcote[6], René Doyon[11], Michael P. Fitzgerald[12], Kate B. Follette[13], Benjamin Gerard[1,2], Alexandra Z. Greenbaum[10,14], Pascale Hibon[15], Sasha Hinkley[16], Bruce Macintosh[13], Patrick Ingraham[17], David Lafrenière[11], Franck Marchis[18], Christian Marois[1,2], Eric L. Nielsen[13,18], Rebecca Oppenheimer[19], Rahul Patel[20], Jenny Patience[21], Marshall Perrin[10], Laurent Pueyo[10], Abhijith Rajan[21], Julien Rameau[11], Anand Sivaramakrishnan[10], David Vega[18], Kimberly Ward-Duong[21], and Schuyler G. Wolff[10,14]
[1] Department of Physics and Astronomy, University of Victoria, 3800 Finnerty Rd., Victoria, BC V8P 5C2, Canada
[2] Herzberg Astronomy & Astrophysics, National Research Council of Canada, 5071 West Saanich Rd., Victoria, BC V9E 2E7, Canada
[3] Department of Astronomy, UC Berkeley, Berkeley, CA 94720, USA
[4] Université Grenoble Alpes/CNRS, Institut de Planétologie et d'Astrophysique de Grenoble, F-38000 Grenoble, France
[5] Department of Astronomy & Astrophysics, University of Toronto, Toronto, ON M5S 3H4, Canada
[6] Dunlap Institute for Astronomy & Astrophysics, University of Toronto, 50 St. George St., Toronto, ON M5S 3H4, Canada
[7] NASA Goddard Space Flight Center, 8800 Greenbelt Rd., Greenbelt, MD 20771, USA
[8] Lawrence Livermore National Lab, 7000 East Ave., Livermore, CA 94551, USA
[9] Subaru Telescope, NAOJ, 650 North Aohoku Pl., Hilo, HI 96720, USA
[10] Space Telescope Science Institute, 3700 San Martin Dr., Baltimore, MD 21218, USA
[11] Institut de Recherche sur les Exoplanètes, Département de Physique, Université de Montréal, Montréal, QC H3C 3J7, Canada
[12] Department of Physics and Astronomy, UCLA, Los Angeles, CA 90095, USA
[13] Kavli Institute for Particle Astrophysics and Cosmology, Stanford University, Stanford, CA 94305, USA
[14] Physics and Astronomy Department, Johns Hopkins University, Baltimore, MD 21218, USA
[15] European Southern Observatory, Casilla 19001, Santiago 19, Chile
[16] University of Exeter, Astrophysics Group, Physics Building, Stocker Rd., Exeter, EX4 4QL, UK
[17] Large Synoptic Survey Telescope, 950 N Cherry Ave., Tucson, AZ 85719, USA
[18] SETI Institute, Carl Sagan Center, 189 Bernardo Ave., Mountain View, CA 94043, USA
[19] American Museum of Natural History, New York, NY 10024, USA
[20] California Institute of Technology, Infrared Processing and Analysis Center, 770 South Wilson Ave., Pasadena, CA 91125, USA
[21] School of Earth and Space Exploration, Arizona State University, PO Box 871404, Tempe, AZ 85287, USA
Received 2016 March 4; revised 2016 May 6; accepted 2016 May 8; published 2016 July 27

ABSTRACT

Using the Gemini Planet Imager, we have resolved the circumstellar debris disk around HD 111520 at a projected range of ~30–100 AU in both total and polarized *H*-band intensity. The disk is seen edge-on at a position angle of 165° along the spine of emission. A slight inclination and asymmetric warp are covariant and alter the interpretation of the observed disk emission. We employ three point-spread function subtraction methods to reduce the stellar glare and instrumental artifacts to confirm that there is a roughly 2:1 brightness asymmetry between the NW and SE extension. This specific feature makes HD 111520 the most extreme example of asymmetric debris disks observed in scattered light among similar highly inclined systems, such as HD 15115 and HD 106906. We further identify a tentative localized brightness enhancement and scale height enhancement associated with the disk at ~40 AU away from the star on the SE extension. We also find that the fractional polarization rises from 10% to 40% from 0.″5 to 0.″8 from the star. The combination of large brightness asymmetry and symmetric polarization fraction leads us to believe that an azimuthal dust density variation is causing the observed asymmetry.

Key words: circumstellar matter – stars: individual (HD 111520)

1. INTRODUCTION

Improved resolution in debris disk imaging has made it possible to uncover many instances of complex morphologies that deviate from the nominally pervasive symmetric ring structures. This offers important insights into the dynamical evolution of the planetary systems, since gaps and asymmetries will result from planet scattering, stellar fly-bys, and ISM interactions (for a review see Matthews et al. 2014, p. 521). Investigations into these important case studies can determine how planetary architectures shape debris disks, or even create them, through planetary stirring of planetesimals (Mustill & Wyatt 2009). Even when the planets themselves may be unseen, important constraints can be made based on the disks' structure (Ertel et al. 2012).

This paper presents resolved imaging from Gemini Planet Imager (GPI) and evidence for strong asymmetry in the disk around HD 111520 (HIP 62657) that is seen from 0.″3 to 1.″0. GPI is an instrument designed to detect scattered light from dust grains and emission from exoplanets in the near-IR at close separations around nearby stars (Macintosh et al. 2014). HD 111520 is an F5V star and has been identified as a member of the Lower Centaurus Crux (LCC) in the Scorpius–Centaurus Association through *Hipparcos* proper motions (de Zeeuw et al. 1999). Stellar parameter estimates have ranged from 6500 to 6750 K for surface temperature, from 2.6 to 2.9 $L_{\odot}$ for luminosity, and 1.3–1.4 $M_{\odot}$ for mass (Houk 1978; Pecaut et al. 2012; Chen et al. 2014). The distance to the system was measured to be 108 ± 12 pc (van Leeuwen 2007), which we adopt throughout this study. The median age of the LCC for F-type stars is 17 ± 5 Myr (Pecaut et al. 2012).

An infrared (IR) excess was first associated with the star by Chen et al. (2011) based on *Spitzer* MIPS data, which derived a

dust radius of 48 AU from a fit to the effective temperature of a single blackbody. In combination with *Spitzer* IRS, multiple temperature components have been fit with grain emissivity models to give an inner disk of 115 K at a radius of 16.3 AU and an outer disk of 51 K at 212 AU (Chen et al. 2014). Subsequent detailed grain model fits have been done to IRS spectra to give estimates of an inner disk at 1 AU and an outer disk of 20 AU (Mittal et al. 2015), although this model greatly underpredicts the 70 μm flux, requiring another outer component. These discrepancies in spectral energy distribution (SED) fitting are primarily due to model degeneracies in the absence of a resolved image of the disk structure. The disk around HD 111520 was first resolved in optical scattered light by *Hubble Space Telescope* (*HST*) to have a large 5:1 brightness asymmetry with emission extending from $\sim$1″ to 5″ (or $\sim$110–550 AU) from the star (Padgett & Stapelfeldt 2015). Indeed, all SED models predict a dust location that is well inside the inner working angle of the discovery *HST* images, but within the GPI field of view (FOV), underlining the importance of GPI for understanding warm debris disk dust. We therefore present GPI data that resolve the disk inside 1″ to better probe the structure of the disk.

2. OBSERVATIONS AND DATA REDUCTION

On the night of 2015 July 2, data were taken as part of the GPI Exoplanet Survey (GPIES; Macintosh et al. 2014). Weather conditions were good, with DIMM (Differntial Image Motion Monitor) seeing at $\sim$1″ and MASS (Multi-Aperture Scintillation Sensor) seeing at $\sim$0.″5. A total of 41 60 s exposures were taken in *H*-band spectral mode ($R \sim 45$), with a total of $\sim$35° of field rotation. In addition, 11 60 s exposures in *H*-band polarization mode were taken for a "snapshot" observation amounting to 7° of rotation. The field rotation allows for angular differential imaging (ADI) to subtract the instrument point-spread function (PSF; Marois et al. 2006). The pixel scale of GPI data is 14.166 $\pm$ 0.007 mas on the sky (updated from Konopacky et al. 2014). The data were reduced using primitives in the GPI Data Reduction Pipeline (see Perrin et al. 2014, and references therein).

For polarimetry mode data, the light is split by a Wollaston prism into two orthogonal linear polarization states that are modulated by a rotating, achromatic half-wave plate. A typical observing sequence involves observations in sets of four different wave plate orientations, which are then combined to produce a Stokes data cube (Perrin et al. 2015). First, the raw frames are dark subtracted and "destriped" using Fourier-filtered raw detector images to remove instrumental microphonic noise (Ingraham et al. 2014a). The microlenslet spot locations from a calibration file are corrected for instrument flexure with a cross-correlation algorithm (Draper et al. 2014). The raw data are then converted to a polarization data cube, where the third dimension contains the two orthogonal polarization states. Systematic variations in the polarization pairs and bad pixels are cleaned by a modified double difference algorithm (Perrin et al. 2014). A geometric distortion correction was also applied (Konopacky et al. 2014). The data are then smoothed by a Gaussian kernel with a width equivalent to a nearly diffraction limited GPI PSF (FWHM = 3 pixels). By measuring the fractional polarization behind the occulted spot, the instrumental polarization is measured and subtracted off from each pixel based on its total intensity (Millar-Blanchaer et al. 2015). Following Hung et al. (2015), flux calibration was performed measuring the photometry of the satellite spots with elongated apertures with a known conversion to compare with the Two Micron All Sky Survey (2MASS) magnitude for the star (7.830 $\pm$ 0.057 mag or 0.756 $\pm$ 0.040 Jy; below 2MASS saturation limits; Cutri et al. 2003). All of the polarization data cubes were then combined via a singular value decomposition method to create a Stokes data cube (Perrin et al. 2014). Finally, the Stokes cube was converted to the radial Stokes convention: $[I, Q, U, V] \rightarrow [I, Q_r, U_r, V]$ (Schmid et al. 2006). The star location, which is used as the origin of the transformation, is measured using a radon transform-based algorithm that takes advantage of the elongated satellite spots (Wang et al. 2014; Pueyo et al. 2015). The final Q_r and U_r images can be seen in Figure 1.

For the spectroscopy mode data, the raw dispersed frames were dark subtracted, corrected for bad pixels, and "destriped" (Ingraham et al. 2014a). A wavelength calibration using an Ar arc lamp was taken just prior to the observations and corrected using a repeatable flexure model of the instrument as a function of telescope elevation (Wolff et al. 2014). In this case, the correction amounted to a negligible change from the nominal wavelength calibration. To extract into a 3D spectral data cube, a box aperture method was used (Maire et al. 2014). There were interpolation errors along the wavelength axis at the blue end of the data cubes, so the first three individual spectral channels (or 0.024 μm bandpass) were removed prior to collapsing the cube. A flat-field image can have a pixel-to-pixel standard deviation on the order of $\sim$10% and therefore cannot explain surface brightness variations above this level. A microlens-PSF method (Draper et al. 2014; Ingraham et al. 2014b) was also used to optimize the flux extraction and reduce spaxel-to-spaxel noise (i.e., spectral pixels). These cubes did not have bad cube slices but yielded similar results for the PSF-subtracted images. To remove persistent bad spaxels, they are identified as being discrepant from a spatial 3×3 box median-filtered image per wavelength slice and then smoothed by assigning it the median value of a $3 \times 3 \times 3$ region within the cube centered on the bad spaxel. The satellite spot locations were identified after high-pass filtering in order to derive the star location under the coronograph for each data cube. The star-centering accuracy is 0.05 pixels for satellite spots with signal-to-noise ratio (S/N) > 20 for spectral data cubes (Wang et al. 2014). Our data have an S/N around 20, which can be up to 0.1 pixels or 1.4 mas in astrometric precision. Finally, the data were flux calibrated using the satellite spots within the image and the target's 2MASS magnitude and spectral type (for bandpass color corrections) into surface brightness (Wang et al. 2014). In all, varying the use of any of these data cube reduction steps did not significantly alter the resulting data cubes to the level of spatial flux variation seen in Section 5. Lenslet flat-fielding tended to introduce more "checkerboard" or spaxel-to-spaxel noise in the data cubes, likely because they were obtained on a different night with a flexure shift causing the microlenslets to sample different pixels on the detector. Therefore, it was left out of the data reduction procedure.

3. PSF SUBTRACTION

The spectral mode cubes require PSF subtraction to remove instrumental scattered light and isolate the astrophysical emission. The spectral mode cubes were combined with pyKLIP (Wang et al. 2015) using the ADI-only mode of

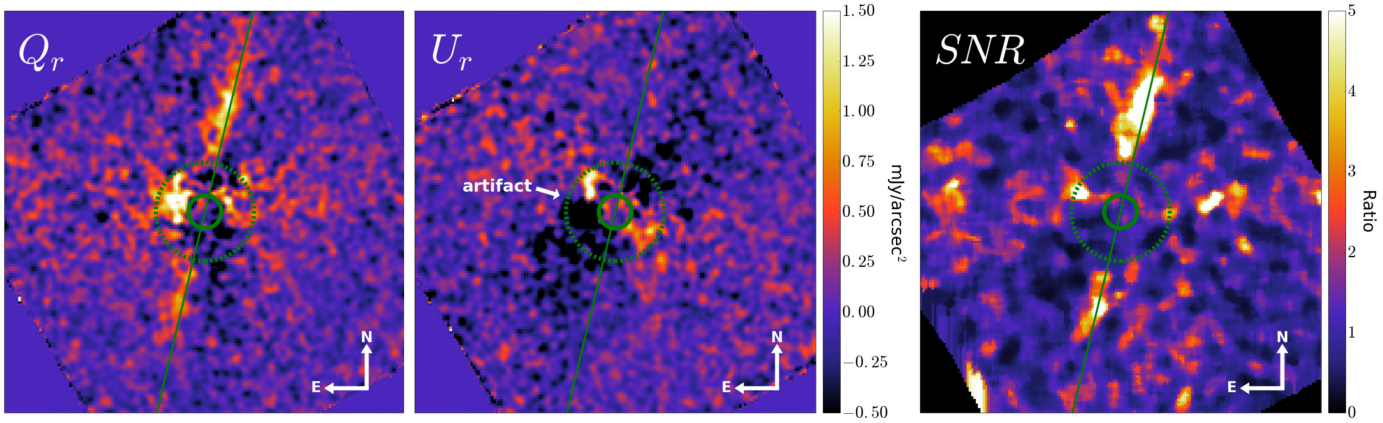

Figure 1. *H*-band radial Stokes polarized intensity. The coronagraph is marked by a solid green circle. The FOV of the images is cropped to $2\farcs4 \times 2\farcs4$. The dashed green circle denotes a region with enhanced noise out to $0\farcs3$ in radius from the center. Left: radial Stokes Q_r showing that the disk emission is aligned along a position angle (PA) of 165° centered at the star, illustrated by the green line. Middle: radial Stokes U_r shows polarized light from nonastrophysical sources (assuming single scattering) and is therefore an estimate of the noise in the data. Both Q_r and U_r images are shown using the same color scale. A large artifact of $\sim 0\farcs1$–$0\farcs3$ to the east of the coronagraph appears in both Q_r and U_r and is therefore likely an instrumental effect. Right: S/N map showing the detection of the disk.

individual spectral channels (Marois et al. 2006). The resulting image from the collapsed cube is shown in the top panel of Figure 2. The KLIP algorithm uses a principal component analysis method, in concert with the angular rotation of the data sets, to determine the best PSF model to subtract (Soummer et al. 2012). Multiple iterations of pyKLIP were median combined to produce the final image using 41 KL mode basis vectors with annuli and angular separations from 5 to 18 equal subdivisions of the image.

In order to confirm that the apparent NW-to-SE asymmetry seen in the pyKLIP reduction was not due to self-subtraction, we also applied a version of pyKLIP that used reference differential imaging. Instead of using the target data set to construct the PSF, this method relied on an extensive broadband PSF library composed of observations of disk- and companion-free reference stars obtained during the GPIES campaign. Broadband images were created either by summing all the wavelength channels in spectroscopy mode data cubes or by summing the two orthogonal polarization states in polarimetry mode data. In this way, data from both observing modes can be used as broadband PSF references. At the time these reductions were carried out, the library consisted of approximately 7400 PSFs. All of the GPIES data cubes were reduced in a similar manner, following the standard reduction recipes (e.g., Section 2). For each spectroscopy mode data cube in the HD 111520 data set, the 100 most correlated PSFs in the library were selected as reference PSFs and then processed using pyKLIP. The reduction used a combination of 3 and 6 pixel annuli and 10 KL modes, with vector lengths ranging from 7 to 49, which were averaged together to smooth out remaining artifacts. The result can be seen in the middle panel of Figure 2. A more detailed description of the broadband PSF library will be discussed further in an upcoming paper (M. A. Millar-Blanchaer et al. 2016, in preparation).

Another method we employed to preserve disk flux consists of subtracting a PSF model, interpolated from data that had the disk masked, before recombining the data set (bottom panel of Figure 2). The method is similar to the PSF subtraction technique used on GPI data of HR 4796A (Perrin et al. 2015). Each spectral cube is summed along its wavelength axis to make a broadband image. A rectangular region encompassing the extent of the disk is masked. The PSF is sampled outside of the masked region to fit a low-order polynomial over the masked regions. The PSF model is smoothed with a median filter and subtracted from each image before recombining the data by derotating into the same frame of reference on the sky. Depending on the normalization, the absolute flux level can vary by ∼30% but does not impart localized surface brightness variations, such that relative differences in surface brightness are preserved.

In general, a pyKLIP-ADI PSF subtraction performs best at subtracting the residual PSF but leads to many artifacts that are not ideal for extended sources (Figure 2). Given the edge-on nature of the disk, disk self-subtraction is present, but is not strong enough to preclude it from detection as it would be for a centrosymmetric face-on disk. Also, ringing and radial spokes are noticeable artifacts of this type of PSF subtraction. The NW-to-SE brightness asymmetry persists when using fewer KL modes but structure in the fainter SE is less apparent. Overall, this method leads to oversubtraction especially on the faint SE extension (compare the different panels of Figure 2). Using a PSF library for references in the reduction greatly enhances the optimal subtraction but still leaves some of the KLIP artifacts. On the other hand, the masked PSF fitting leads to the least subtraction of the disk, though at the cost of a slightly larger inner working angle where residual artifacts dominate. We therefore use the latter method to measure the disk's surface brightness and morphology. Since the polarization mode data set has fewer observations and less parallactic rotation, we use the spectral mode data to constrain the total intensity. Through flux calibration between both modes, we can compare the polarized intensity to the total intensity to get fractional polarization.

In the polarization mode with GPI, it is possible to isolate scattered light from a disk that is polarized and thereby remove the instrumental PSF that is assumed to be unpolarized. Light that scatters from optically thin dust around the star will have an electric field vector that is oriented centrosymmetrically around the star (parallel or orthogonal to rays emanating from the star), while residual polarized instrumental noise can have other orientations. In some cases optical depth effects, grain properties, and viewing geometry may impact this conclusion, but it is robust for optically thin disks (Canovas et al. 2015). As expected, the disk can be clearly seen in Q_r with similar morphology to the total intensity (Figures 1 and 2). The U_r

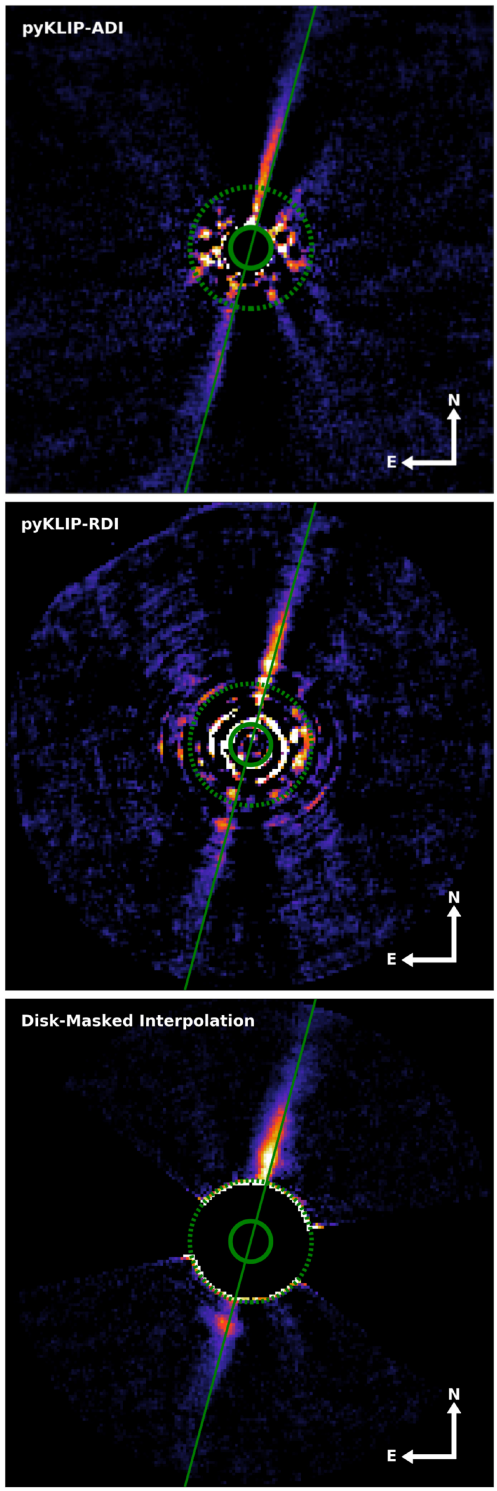

Figure 2. Collapsed *H*-band spectral mode data reduced using various PSF subtraction methods. The FOV of the images is cropped to $2\farcs4 \times 2\farcs4$. Top: reduced with an ADI-only reduction with pyKLIP. Middle: PSF-subtracted data using a PSF library from GPI Exoplanet Survey data as a reference for a pyKLIP reduction. Bottom: PSF-subtracted by interpolating over disk-masked data as done in Perrin et al. (2014). The solid green circle denotes $0\farcs1$, which is obstructed by the coronagraph. The dashed green circle denotes a $0\farcs3$ radius inside of which large artifacts are present in all of the PSF reductions. The solid line denotes the primary plane of the disk major axis of the emission along a PA of 165°.

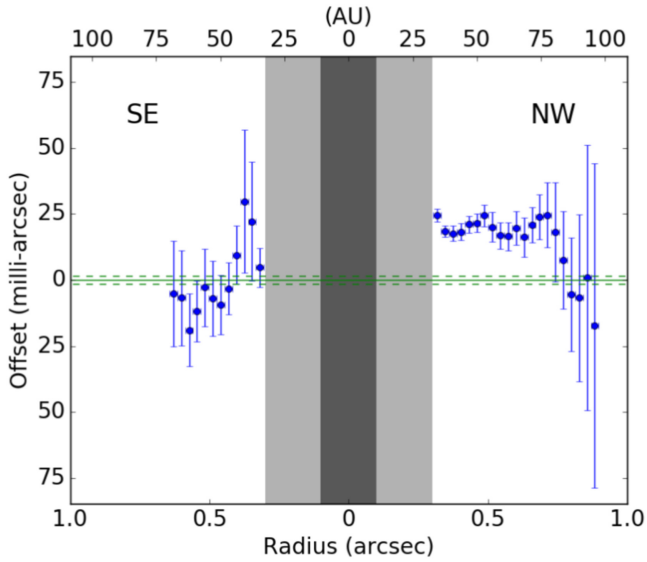

Figure 3. Vertical location of the peak disk emission along the spine relative to a line PA of 165° centered on the star. The light-gray region indicates the region dominated by noise within $0\farcs3$, and the dark-gray area shows the region under the chronograph at $0\farcs1$ (See Figure 2). The dashed green lines represent an upper limit on the uncertainty in the stellar position of 1.4 mas. The disk emission does not appear to be arced, as would be the case for a symmetric ring slightly inclined from exactly edge-on, given the precision of our measurements (indicated by the FWHM/S/N as error bars). The slight offset we observe may nonetheless result from a few-degree inclination of a closed ring disk, if the ring radius is significantly larger than the GPI FOV. Alternatively, a small warp producing an "S" shape may be present but, given the brightness asymmetry, would not be as apparent. A localized offset on the SE extension, though, is apparent just inside 50 AU, corresponding to an enhanced surface brightness feature (see Figure 5).

image, however, shows correlated noise that we assume to be instrumental in origin just east of the coronagraph between $0\farcs1$ and $0\farcs3$. The disk itself seen in Q_r stands out above the noise shown in U_r in relative strength and location.

4. MORPHOLOGY

In order to measure midplane variations of the disk, we fit a functional profile to the disk emission. It can be seen in Figure 2 that all of the PSF subtraction methods show the disk in total intensity. It appears near an inclination of 90° and centered on the star. We have added a green reference line passing through both the north and south extensions of the disk. We rotate the PSF-subtracted image by 75° clockwise to orient the disk horizontally and to measure the disk emission along the spine relative to the green line at a position angle (PA) of 165°. A Cauchy function (Equation (1)) was fit to the surface brightness (I), with a brightness offset (I_o) and constant (C). This technique and function have been used before on edge-on disks such as AU Mic (Graham et al. 2007). The function was fit along each vertical slice of the disk (about 30 pixels wide) in the x direction, perpendicular to the disk axis, to measure the location of the central spine of emission (x_o) and its FWHM ($\sim 2h$):

$$I = \frac{C \times h}{\pi \times (h^2 + (y - y_o)^2))} + I_o. \quad (1)$$

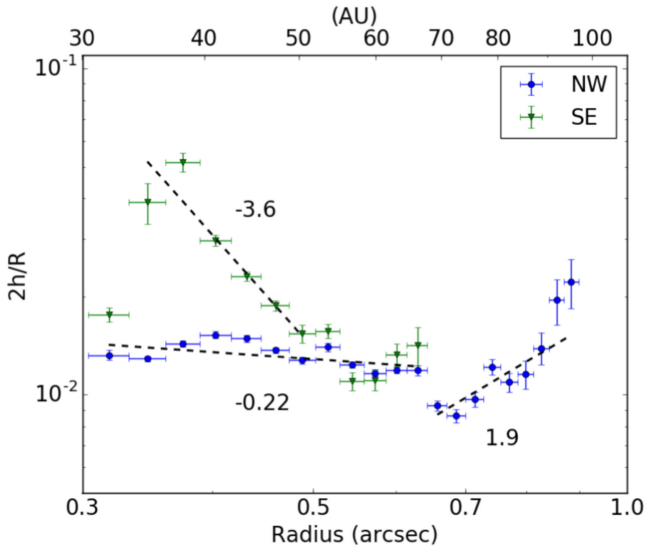

Figure 4. Effective vertical FWHM of the disk as a function of stellocentric radius. Green points are the SE extension, and blue points are the NW extension. The exponent for each respective power-law fit is displayed near the fitted line. An enhancement of the SE extension's scale height relative to the NW extension can be seen inside 50 AU (or ∼0.″5). Outside that point, it returns to a similar power law with distance. Unlike the SE extension, the NW extension is still detected beyond 0.″7 and appears to transition to a positive slope.

Figure 3 shows the disk midplane measurements deviating from $y_0 = 0$, indicating disk structure from inclination, warping, or both. The ∼18 mas offset is significant compared to the upper limit of 1.4 mas astrometric precision. On the SE extension there is a localized offset at 40 AU. If the disk were a symmetric ring inclined close to edge-on, we should see an arc in the disk from one extension to the other (e.g., Mazoyer et al. 2014; Figure 5), while if it were perfectly edge-on, we should see a flat zero offset for the entire length of the disk through the star's position (Kalas & Jewitt 1995). The deviation in emission along the spine was not significant enough to measure an arc in the disk. Examination leads us to conclude that the disk PA is 165° measured to the major disk axis east of north. If the general offset on the NW extension of the disk is the result of an inclined disk relative to our line of sight, then the offset of the spine of disk emission relative to a line centered through the star would translate to ∼1.°3–1.°7 (assuming a disk ring radius of 70–90 AU), making the disk inclination ∼88° instead of 90°. Since inclination and disk PA can be covariant given these assumptions, they represent general estimates rather than rigorously modeled parameters. The lateral asymmetry again makes it difficult to distinguish between a warp, offset, and/or inclination.

Furthermore, we examine the projected scale height distribution as a function of separation, in Figure 4. A scale height enhancement can be seen at the same location as the localized offset in the SE extension inside 50 AU, indicating that there is some structure to the disk. The scale height is measured from the peak emission and independent of any offset. If the disk is inclined, then scale height in this case is rather a projection of emission on the front and back side of the disk. It can be seen that the two sides have different slopes interior to about 0.″5 and then have a common slope up until 0.″65, where the emission on the SE is noise dominated, but the NW extension appears to change to a positive slope in scale height, suggesting that a transition in the disk emission is occurring around 70 AU, which could be indicative of the location of the disk ansae (Graham et al. 2007). While the SE disk blob is present in two different PSF subtraction routines, the possibility remains that this observation may be a spurious artifact from emission that is arcing with parallactic rotation close to the noise-dominated region inside 0.″3.

5. SURFACE BRIGHTNESS DISTRIBUTION

In order to determine the brightness of the disk, we again use the masked PSF-subtracted images as this results in the least self-subtraction of the disk. We rotate the PSF-subtracted image from the disk-masked interpolation method by 75° to orient the disk horizontally within the image to measure the radial surface brightness of the disk (Figure 5). Using rectangular apertures 7 pixels wide in the y (vertical) direction (which is approximately twice the FWHM of a GPI PSF), we measure the surface brightness as a function of distance along the spine of the disk and the standard deviation in each aperture. The data were binned by averaging every 5 pixels in the x (horizontal) direction with the errors added in quadrature. The noise floor of each image is independently estimated by performing the same operation at a PA 45° away from the disk. Points that are above the red line indicate that the signal in the disk is significant. We find an asymmetry between the SE side and the NW side of the disk in total intensity, where the peak intensity on the NW side of the disk is a ratio of 2:1 brighter than the SE side (left panel of Figure 5). The polarized intensity is also about a ratio of 2:1 brighter on the NW side (right panel of Figure 5). Compared to other debris disks, it is one of the most extreme cases of brightness asymmetry as measured at projected separations interior to the inferred ring radius (see Sections 4 and 6).

Overall, the total intensity on the NW side has a smooth decline with radius. The SE side, however, appears to have a resolved peak near 40 AU, the same location as the scale height enhancement. The NW side similarly appears to flatten around 45–50 AU before being dominated by noise at the inner working angle. In the polarized intensity, the surface brightness has a pronounced peak stretching from 50 to 75 AU. Different behaviors are expected in the profiles of total intensity and polarized intensity in the context of a ring made of predominantly forward-scattering dust grains. The total intensity along an edge-on disk will be continuously declining with projected separation, with a sharp drop-off outside the disk ansae. In contrast, the polarized light may peak in intensity toward increasing scattering angle from the disk. However, this depends on the phase function and the surface density distribution with radius as these two quantities are covariant in total intensity.

With combined total intensity and polarized intensity, it is possible to measure the fractional polarization as a function of separation from the star. In Figure 6, it can be seen that, despite the surface brightness asymmetry, the two extensions of the disk follow roughly the same trend upward to 30% polarization at 70 AU. Data are excluded if the combined S/N is within 3σ of zero to show only robust detections of the fractional polarization. This largely affects the regions outside the main peaks of polarized intensity from around 50 to 75 AU, as the noise is dominated by the lower S/N of the polarized intensity detection. A rise in polarization fraction is likely due to a rise toward peak scattering angle near the ansae from an annular

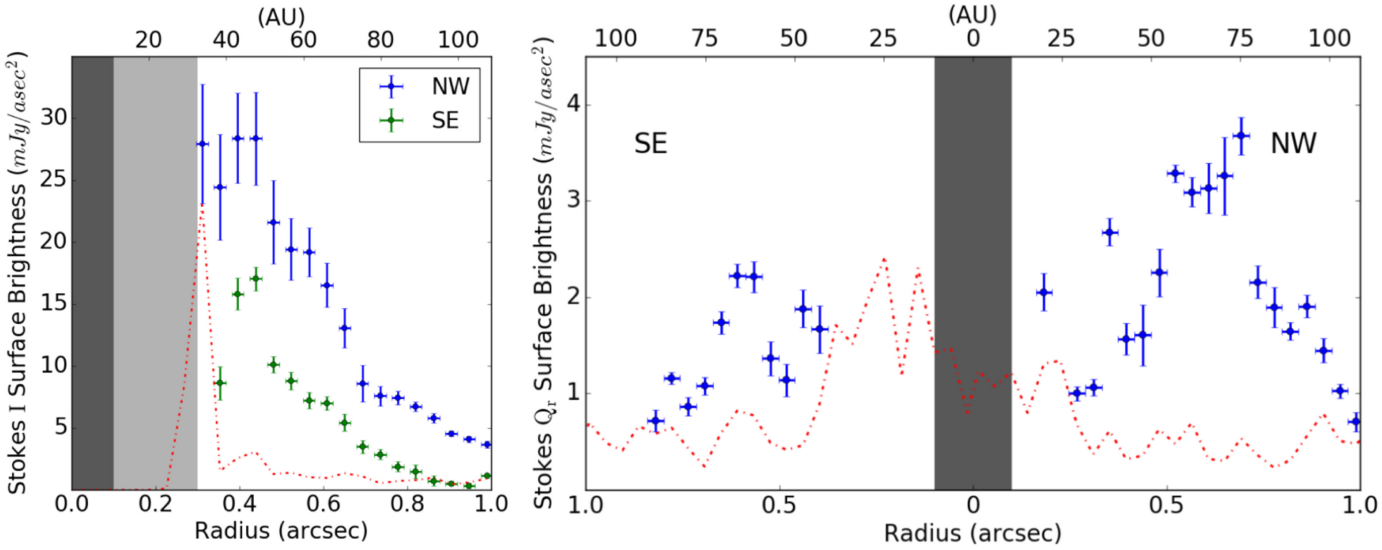

Figure 5. *H*-band surface brightness profiles for the combined spectral mode data in total intensity (left panel) and in polarized intensity (right panel). The blue and green dots denote the respective surface brightnesses of 7-pixel-wide apertures with standard deviation error bars binned over 5 pixels. The horizontal error bars show the extent of the binned regions. The dotted red line denotes a noise floor. For total intensity, that is mean plus a 1σ standard deviation in regions of the data without a disk (45° away from the disk midplane). In polarized intensity, it is the same, except using the U_r image cospatial with the Q_r data. The dark-gray region demarks the area under the coronagraph. The light-gray area shows the region inside of the dotted green circle in Figure 2, where artifacts from PSF subtraction are apparent.

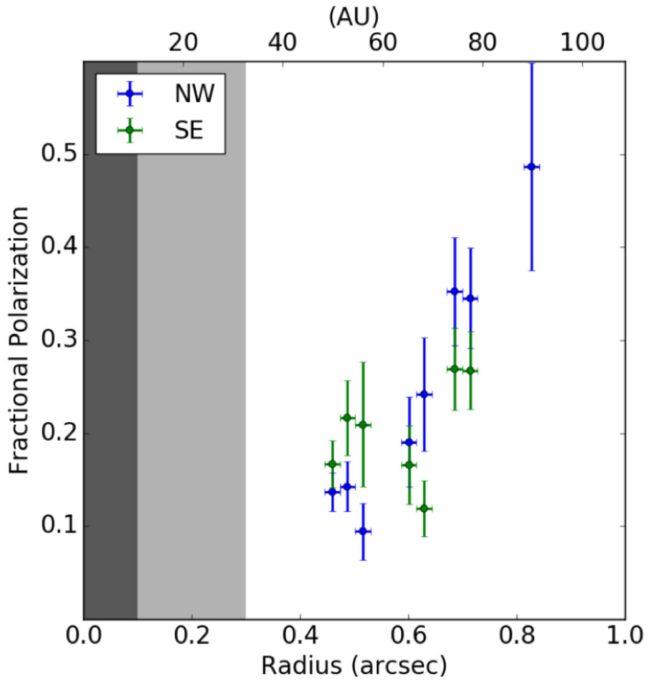

Figure 6. Polarization fraction as measured between the spectral mode and polarization mode of GPI. Blue points indicate the NW extension, and green points indicate the SE extension of the disk. The polarization fraction trends upward from ≈0.1 to ≈0.4 in the range of 40–80 AU. Error bars indicate the combined S/N of the spectral mode and polarization mode. Both extensions appear to have similar distribution of fractional polarization with separation from the star given the precision of the current measurements. The polarized intensity dominates the error given a short observing sequence. Data in regions with total $S/N < 3$ are excluded to illustrate where we can confidently measure a fractional polarization. The dark-gray region is the region covered by the coronograph, and the light-gray region is an area dominated by PSF subtraction artifacts (see Figure 2).

disk with an inner gap (Graham et al. 2007). However, the S/N of our images is insufficient to assess whether a plateau in polarization fraction is achieved within GPI's FOV.

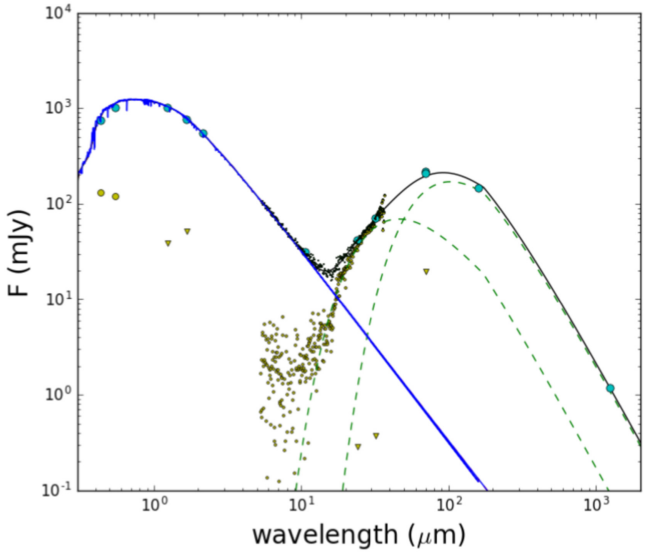

Figure 7. SED for HD 111520. Archival photometry is in cyan. The black line is the total fit to the data. The blue line is a stellar Kurucz model. The two green dashed lines are the modified blackbody dust components. Yellow points denote the residuals of the SED fit, with inverted triangles being within measurement uncertainty. *Spitzer* IRS spectra are seen as black points.

6. SPECTRAL ENERGY DISTRIBUTION

In order to provide context for the GPI observations, we fit an SED model to archival photometry of HD 111520 (Figure 7). Photometry included the optical Tycho-2 survey (Høg et al. 2000) and infrared surveys from 2MASS (Cutri et al. 2003) and *Spitzer* (Chen et al. 2014). Public archival *Herschel* PACS (Poglitsch et al. 2010) observations (Obs. ID 1342227022-23; PI D. Padgett) and ALMA Cycle 1 Band 6 (1.3 mm) continuum observations (Proj. ID 2012.1.00688.S; PI J. Carpenter) were measured with aperture photometry to better constrain the cold component of the SED (Table 1). *Herschel* PACS data were reduced with the standard HIPE pipeline

Table 1
Additional Photometry from Archival Observations

Instrument	Effective Wavelength (μm)	Flux (mJy)
Herschel PACS	70	205 ± 4
Herschel PACS	160	145 ± 6
ALMA Band 6	1252	1.17 ± 0.08

(Ott 2010) and were measured with 12″ and 22″ circular apertures for 70 and 160 μm with aperture flux correction factors of 0.8 and 0.82, respectively. ALMA continuum maps were retrieved from the ALMA Science Archive and were measured with a 2.″5 aperture. The rms error was estimated from random apertures of the same size placed in the FOV. Images of the emission associated with HD 111520 can be seen in Figure 8. Whereas the data are consistent with a point source at 70 μm, there is some extended emission at 160 μm, and therefore our aperture photometry leads to an overestimate of the 160 μm flux associated with HD 111520. A second point source is detected in the ALMA map at a PA of 329°, 11.″9 away from the peak emission of HD 111520 with a flux density of 0.5 mJy. That second source may contribute to the extended emission we see at 160 μm. It may also be from a background object, but given the perturbed nature of the disk, it is conceivable that it is dynamically relevant, if it were found to be comoving at a separation of ~1200 AU.

Magnitudes were converted to mJy using the zero points of the respective instruments. *Spitzer* MIPS and *Herschel* PACS have complementary measurements at 70 μm and are consistent within 1σ uncertainties. A Kurucz model was fit to the predominately stellar photometry ($\lambda < 10$ μm) in Figure 7 with an effective temperature of 6750 K. The star-subtracted flux densities were then least-squares fit with two modified blackbody SEDs using the photometric uncertainties as weights. The emission is modified by a power law to model the inefficient emission from grains much smaller than the observed wavelength (Wyatt 2008). The modified slope parameters include a knee at 173 μm with a β index of 0.8, but given the lack of photometric coverage near the knee, both parameters remain uncertain. Two components are necessary in order to provide a good fit to all of the data at $\lambda > 10$ μm. The temperatures of the warm and cold components in the SED are measured to be 111 ± 2 K and 49 ± 2 K, respectively. Uncertainties were determined using the diagonal of the covariance matrix and therefore do not necessarily represent systemic biases such as non-blackbody grains.

This new SED fit is unique compared to previous SED fitting in that it includes the far-IR observations from *Herschel*, which tightly constrain the temperature of the cold dust component. Given a stellar luminosity of 2.9 $L_{\odot}$ and assuming blackbody temperatures for the dust, we find implied disk radii of 11 and 54 AU, respectively, from simple scaling relations (Wyatt 2008). Given that an 11 AU disk component would be completely under the coronograph or dominated by noise, we are mostly resolving emission stemming from the cold component disk. If the polarized intensity and scale height trends are indicating that the disk radius is near 70 AU, and if the scattered light is tracing the population of larger grains from thermal emission, then the disk radius measurements are reasonably consistent. Since small dust grains are not perfect blackbodies, it is not surprising that the actual resolved scattered light radius is larger than the inferred disk radius from the SED fitting (Booth et al. 2013). The $R_{\rm disk}/R_{\rm BB}$ ratio has been found to scale with luminosity due to radiation pressure more effectively blowing out the smaller grains, which have non-blackbody behavior (Morales et al. 2013). Applying these relations to this star, we would expect the $R_{\rm disk}$ to be 2–3 times that measured by the SED, which is about 108–162 AU, or right at the edge of the GPI FOV.

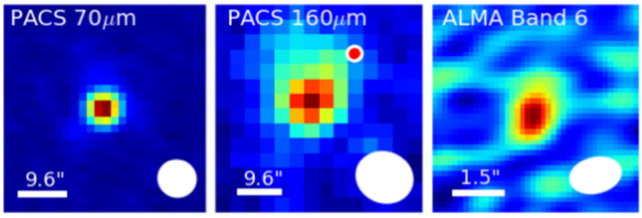

Figure 8. Images from *Herschel*/PACS and ALMA showing detections of emission from HD 111520 within their respective wavelengths. The white bars are for image scale, and the white ellipses show the respective beam sizes. At PACS 70 μm and ALMA 1252 μm the emission is seen as a point source, while at PACS 160 μm there are hints of extended emission to the N side, possibly stemming from the disk, but possibly due to confusion with other background sources. The location of the second ALMA source is plotted as a red dot in the PACS 160 μm image. The 160 μm emission seems elongated in a similar direction to the second source, though clearly not all of the flux contamination would be from that source specifically. Note that the ALMA image is shown on a different scale than the PACS observations to best show the emission from HD 111520 and therefore does not reveal the second source.

7. DISCUSSION

The discovery *HST* optical images of the HD 111520 disk revealed a nearly perfectly edge-on disk with a strong 5:1 brightness asymmetry (Padgett & Stapelfeldt 2015). Our new *H*-band GPI observations reveal that this asymmetry extends well within the inner working angle of *HST*, with a 2:1 asymmetry from 0.″3 to 1.″0. A possible localized brightness enhancement in total intensity at 40 AU is seen on the SE side with two PSF subtraction methods. Explanations for this brightness asymmetry could include a localized variation in dust properties, optical depth effects, or strong density perturbations.

Variations in the dust grain scattering efficiency could cause a variation in brightness if perhaps there were two distinct grain populations on either side of the disk. However, the symmetry of the polarization fraction curve between the two extensions suggests that the dust properties are similar on both ansae. Another possibility is that the dust grains themselves might be at slightly different stellocentric distances resulting from an eccentric disk, possibly induced by a perturbing planet (Wyatt et al. 1999). A small brightness asymmetry in thermal emission would then result from the pericenter glow, with the brighter side being closer. A similar effect would be observed in scattered light, as shown in potential models of HD 106906 (Kalas et al. 2015). The peak polarized emission on the NW is slightly farther out than the SE side in polarized intensity, suggesting some eccentricity even if we cannot resolve the ansae explicitly. If the disk were eccentric, however, it would cause a brightening on the SE extension rather than the NW extension. Therefore, the observed brightness asymmetry cannot be ascribed to localized differences in dust grain properties or disk eccentricity.

Another possibility to consider is that we may just be seeing optical depth effects in the scattered dust. It might be the case that the dust in the outer disk is not asymmetrical, but rather

appears that way through disk shadowing. If the inner disk (hotter component) were asymmetrical in scale height, were misaligned relative to the outer disk, or had a locally enhanced density, it could be preferentially shadowing the SE part of the disk. This could occur without needing to invoke a density asymmetry in the outer disk, similar to what is seen in denser protoplanetary disks (Dullemond et al. 2001; Wisniewski et al. 2008). The fractional luminosity of the excess emission ($L_{\rm IR}/L_* \approx 10^{-3}$), however, suggests that the scattered light is optically thin and inconsistent with this idea. Some observations suggest that debris disks can still be optically thick in the near-IR such as with HR 4796A (Perrin et al. 2015). In such cases the vertical scale height and width may be narrow enough that a low-mass disk could cause shadowing. However, this would be a transient phenomenon as it would tend to diffuse dynamically into a more diffuse ring. It may be possible to monitor changes in the inner disk from near-IR variability in concert with scattered light observations to test for transient disk morphology.

If there are density perturbations in the disk such as azimuthal gaps or spirals, when projected at an inclination of 90°, it would cause a similar brightness variation to what is observed. This would be hard to determine conclusively given our limited viewing angle on the system. HD 111520 itself is an extremely wide binary at a separation of ∼159″ (or ∼17,000 AU) at a PA of 78° identified through common proper motion (Mason et al. 2012). Spiral features induced by a binary star are unlikely, since the co-orbital timescale would be much larger than the orbital timescale of the disk. Smaller mass pertubers have also been searched for with NICI, which did not find any low-mass companions within 0.″5–5″ (Janson et al. 2013). It may also be that there is an increased density on the NW side from a recent large collision diffusing small grains, as is seen in β Pic, for instance (Dent et al. 2014). Although the submillimeter flux in that case traces the larger grains of the dust, we see light being scattered from smaller grains with GPI.

A few other such systems have been found with similar brightness asymmetries. For example, HD 15115 was discovered to be asymmetric by *HST* (Kalas et al. 2007). Using forward modeling of the disk with NICI data, Mazoyer et al. (2014) were able to show that the disk morphology is in fact ring-like at a radius of 90 AU, with the east-west asymmetry possibly stemming from either a local over-/underdensity or variation in grain properties. It is also thought that an ISM interaction or recent collision of bodies could have occurred and changed the density or size distribution of grains. Another example is HD 106906, which was also shown to be asymmetric in *HST* data. Images from GPI (Kalas et al. 2015) and SPHERE (Lagrange et al. 2016) show a brightness asymmetry from a near edge-on disk. The variation in brightness is on the order of ∼20% for the total intensity and polarized intensity. A disk that is eccentric, offset, or both could explain these levels of brightness asymmetry. Since HD 106906 also has a wide-orbit planetary companion, it is possible that the dynamical activity between the disk and planet causes this asymmetry. HD 111520, on the other hand, has a strong asymmetry throughout the disk (from 5:1 to 2:1), which proves much harder for similar arguments to explain surface brightness variations of that magnitude. In comparison to the other examples, HD 111520 is the most extreme "needle-like" disk yet observed.

Given the current data set, it remains impossible to conclusively determine a cause until a more complete picture can be formed through continued monitoring of the system. What we can determine is that the brightness asymmetry is strong, by a factor of a few, relative to other "needle"-like debris disks, which are on the order of tens of percent. Furthermore, it persists from *HST* observations down to GPI's FOV. The clump on the SE side will also have to be confirmed and characterized to know whether it is relevant to the disk structure. Since the disk has a consistent polarization fraction with distance on both sides, a likely scenario is that a large disruption event from a stellar fly-by or planetary perturbations altered the disk density and therefore surface brightness, rather than dust grain inhomogeneities. Through more data of peculiar systems, such as HD 111520, we can determine the true nature and evolution of exo-solar systems.

Based on observations obtained at the Gemini Observatory, which is operated by the Association of Universities for Research in Astronomy, Inc., under a cooperative agreement with the National Science Foundation (NSF) on behalf of the Gemini partnership: the NSF (United States), the National Research Council (Canada), CONICYT (Chile), the Australian Research Council (Australia), Ministério da Ciência, Tecnologia e Inovação (Brazil), and Ministerio de Ciencia, Tecnología e Inn.

This paper makes use of the following ALMA data: ADS/JAO.ALMA #2012.1.00688.S. ALMA is a partnership of ESO (representing its member states), NSF (USA), and NINS (Japan), together with NRC (Canada), NSC and ASIAA (Taiwan), and KASI (Republic of Korea), in cooperation with the Republic of Chile. The Joint ALMA Observatory is operated by ESO, AUI/NRAO, and NAOJ. The National Radio Astronomy Observatory is a facility of the National Science Foundation operated under cooperative agreement by Associated Universities, Inc.

This research has made use of the SIMBAD database, operated at CDS, Strasbourg, France.

Z.H.D. and B.C.M. acknowledge a Discovery Grant and Accelerator Supplement from the Natural Science and Engineering Research Council of Canada.

Supported by NSF grants AST-0909188, AST-1313718 (J. R.G., J.J.W., P.G.K.), AST-141378 (G.D., M.F.), and AST-1411868 (K.F., J.L.P., A.R., K.W.D.).

Supported by NASA grants NNX15AD95G/NEXSS, NNX14AJ80G, and NNX11AD21G (J.R.G., J.J.W., P.G.K.).

Portions of this work were performed under the auspices of the U.S. Department of Energy by Lawrence Livermore National Laboratory under Contract DE-AC52-07NA27344 (S.M.A.).

Facility: Gemini:South.

REFERENCES

Booth, M., Kennedy, G., Sibthorpe, B., et al. 2013, MNRAS, 428, 1263
Canovas, H., Ménard, F., de Boer, J., et al. 2015, A&A, 582, L7
Chen, C. H., Mamajek, E. E., Bitner, M. A., et al. 2011, ApJ, 738, 122
Chen, C. H., Mittal, T., Kuchner, M., et al. 2014, ApJS, 211, 25
Cutri, R. M., Skrutskie, M. F., van Dyk, S., et al. 2003, yCat, 2246, 0
de Zeeuw, P. T., Hoogerwerf, R., de Bruijne, J. H. J., Brown, A. G. A., & Blaauw, A. 1999, AJ, 117, 354
Dent, W. R. F., Wyatt, M. C., Roberge, A., et al. 2014, Sci, 343, 1490
Draper, Z. H., Marois, C., Wolff, S., et al. 2014, Proc. SPIE, 9147, 4
Dullemond, C. P., Dominik, C., & Natta, A. 2001, ApJ, 560, 957
Ertel, S., Wolf, S., & Rodmann, J. 2012, A&A, 544, A61

Graham, J. R., Kalas, P. G., & Matthews, B. C. 2007, ApJ, 654, 595
Høg, E., Fabricius, C., Makarov, V. V., et al. 2000, A&A, 355, L27
Houk, N. 1978, Michigan Catalogue of Two-dimensional Spectral Types for the HD Stars (Ann Arbor, MI: Univ. of Michigan)
Hung, L.-W., Duchêne, G., Arriaga, P., et al. 2015, arXiv:1511.06767
Ingraham, P., Perrin, M. D., Sadakuni, N., et al. 2014a, Proc. SPIE, 9147, 7
Ingraham, P., Ruffio, J.-B., Perrin, M. D., et al. 2014b, Proc. SPIE, 9147, 91477K
Janson, M., Lafrenière, D., Jayawardhana, R., et al. 2013, ApJ, 773, 170
Kalas, P., Fitzgerald, M. P., & Graham, J. R. 2007, ApJL, 661, L85
Kalas, P., & Jewitt, D. 1995, AJ, 110, 794
Kalas, P. G., Rajan, A., Wang, J. J., et al. 2015, ApJ, 814, 32
Konopacky, Q. M., Thomas, S. J., Macintosh, B. A., et al. 2014, Proc. SPIE, 9147, 84
Lagrange, A.-M., Langlois, M., Gratton, R., et al. 2016, A&A, 586, L8
Macintosh, B., Graham, J. R., Ingraham, P., et al. 2014, PNAS, 111, 12661
Maire, J., Ingraham, P. J., De Rosa, R. J., et al. 2014, Proc. SPIE, 9147, 85
Marois, C., Lafrenière, D., Doyon, R., Macintosh, B., & Nadeau, D. 2006, ApJ, 641, 556
Mason, B. D., Hartkopf, W. I., & Friedman, E. A. 2012, AJ, 143, 124
Matthews, B. C., Krivov, A. V., Wyatt, M. C., Bryden, G., & Eiroa, C. 2014, Protostars and Planets VI, ed. H. Beuther, R. S. Klessen, C. P. Dullemond, & T. Henning (Tucson, AZ: Univ. of Arizona Press), 521
Mazoyer, J., Boccaletti, A., Augereau, J.-C., et al. 2014, A&A, 569, A29
Millar-Blanchaer, M. A., Graham, J. R., Pueyo, L., et al. 2015, ApJ, 811, 18
Mittal, T., Chen, C. H., Jang-Condell, H., et al. 2015, ApJ, 798, 87
Morales, F. Y., Bryden, G., Werner, M. W., & Stapelfeldt, K. R. 2013, ApJ, 776, 111
Mustill, A. J., & Wyatt, M. C. 2009, MNRAS, 399, 1403
Ott, S. 2010, in ASP Conf. Ser. 434, Astronomical Data Analysis Software and Systems XIX, ed. Y. Mizumoto, K.-I. Morita, & M. Ohishi (San Francisco, CA: ASP), 139
Padgett, D., & Stapelfeldt, K. 2015, in IAU Symp. 314, Young Stars and Planets near the Sun, ed. J. H. Kastner, B. Stelzer, & S. A. Metchev (Cambridge: Cambridge Univ. Press), 175
Pecaut, M. J., Mamajek, E. E., & Bubar, E. J. 2012, ApJ, 746, 154
Perrin, M. D., Duchene, G., Millar-Blanchaer, M., et al. 2015, ApJ, 799, 182
Perrin, M. D., Maire, J., Ingraham, P., et al. 2014, Proc. SPIE, 9147, 3
Poglitsch, A., Waelkens, C., Geis, N., et al. 2010, A&A, 518, L2
Pueyo, L., Soummer, R., Hoffmann, J., et al. 2015, ApJ, 803, 31
Schmid, H. M., Joos, F., & Tschan, D. 2006, A&A, 452, 657
Soummer, R., Pueyo, L., & Larkin, J. 2012, ApJL, 755, L28
van Leeuwen, F. 2007, A&A, 474, 653
Wang, J. J., Rajan, A., Graham, J. R., et al. 2014, Proc. SPIE, 9147, 55
Wang, J. J., Ruffio, J.-B., De Rosa, R. J., et al. 2015, pyKLIP: PSF Subtraction for Exoplanets and Disks, Astrophysics Source Code Library, ascl:1506.001
Wisniewski, J. P., Clampin, M., Grady, C. A., et al. 2008, ApJ, 682, 548
Wolff, S. G., Perrin, M. D., Maire, J., et al. 2014, Proc. SPIE, 9147, 7
Wyatt, M. C. 2008, ARA&A, 46, 339
Wyatt, M. C., Dermott, S. F., Telesco, C. M., et al. 1999, ApJ, 527, 918